scientific reports

Check for updates

OPEN

All-optical switching in epsilon-near-zero asymmetric directional coupler

Yanhua Sha[1], Ze Tao Xie[1], Jiaye Wu[2], H. Y. Fu[3] & Qian Li[1]✉

We propose an all-optical switch based on an asymmetric directional coupler structure with epsilon-near-zero (ENZ) layer. The nonlinear optical properties the of ENZ layer are analyzed by hot-electron dynamics process, and the all-optical operating performance of the switch on the silicon nitride platform is investigated. It is found that the pump-induced refractive index change in ENZ layer gives rise to a transfer of signal light in the optical system. We demonstrate that the proposed switch design features an insertion loss of < 2.7 dB, low crosstalk of < – 18.93 dB, and sub-pico-second response time at the communication wavelength of 1.55 μm. With ultrafast response, high performance, and simple structure, the device provides new possibilities for all-optical communication and signal processing.

Exploration of on-chip optical computing and signal processing has emerged in chip-scale all-optical compute-and-store system[1] and advanced all-optical neurosynaptic network[2]. As fundamental elements, optical logic gates play an important role in complex integrated photonic systems and achieve significant improvements in speed and power consumption of very large-scale integrated photonics. In conventional silicon-based switches, the control mechanism is mainly refractive index change due to two-photon absorption-induced optical Kerr nonlinearity[3]. However, such devices suffer from high-power consumption and large footprint. These drawbacks can be overcome by designed resonance structures, namely, micro-ring resonators[4], photonic crystals[5], etc. Yet, resonance structures are inevitably accompanied by the narrow optical bandwidth and the high demand for fabrication tolerance. To mitigate the disadvantages of silicon photonics, a variety of novel materials integrated with silicon platforms have been demonstrated, such as two-dimensional materials (graphene[6], black phosphorus[7], transition metal dichalcogenides[8]) and phase-change materials ($Ge_2Sb_2Te_5$[9] and VO_2[10]).

In the recent two decades, transparent conductive oxide (TCO) such as indium tin oxide (ITO)[11], aluminum-doped zinc oxide (AZO)[12], cadmium oxide (CdO)[13] have attracted considerable interest in epsilon-near-zero (ENZ) spectral region. Such media exhibit a vanishing permittivity at ENZ wavelength, giving rise to a series of new physical phenomena[14], such as enhanced electric field[15], large optical nonlinearity[11], ultrashort pulse interaction[16], etc., and advanced applications including electro-optical modulator[17,18], all-optical switch[19], perfect absorber[13], etc. For all-optical switching, ENZ TCO materials also have several advantages, such as greater refractive index change by pump excitation, ultrafast response time[11], and intraband optical excitation[13]. These characteristics of ENZ TCO can provide possibilities for breaking the limitations of traditional all-optical waveguide logic gates. To date, all-optical ENZ switches are mostly based on metasurfaces[20,21] or bulk[22] structures, and the reported ENZ-related all-optical waveguide devices are mainly phase modulation designs[23,24]. Therefore, it is necessary to explore its form as all-optical switch in integrated photonic systems.

Here, we propose an all-optical switching scheme of an asymmetric directional coupler (ADC) structure, in which high mobility TCO material (dysprosium-doped CdO) and a pump excitation path are opted to achieve ultrafast and efficient all-optical switching. We analyze the thermal excitation and transient response of the ENZ TCO by employing the non-parabolic conduction band model and the two temperature model (TTM). The two-waveguide optical system consists of an input waveguide and a TCO-loaded waveguide, and the signal light is launched into the input waveguide. The ENZ TCO layer remains low index and lossy without pump irradiation, thus the TCO-loaded waveguide has minimal optical field confinement, resulting in a tendency for light to stay and propagate in the input waveguide. When the pump is irradiated to the ENZ TCO layer at 40 degrees off-normal, the TCO layer is triggered to have a high refractive index and a low absorption coefficient. Therefore, the TCO-loaded waveguide has large optical confinement to accomplish the coupling and transmission. This

[1]School of Electronic and Computer Engineering, Peking University, Shenzhen 518055, China. [2]École Polytechnique Fédérale de Lausanne (EPFL), STI-IEM, 1015 Lausanne, Switzerland. [3]Tsinghua Shenzhen International Graduate School, Tsinghua University, Shenzhen 518055, China. ✉email: liqian@pkusz.edu.cn

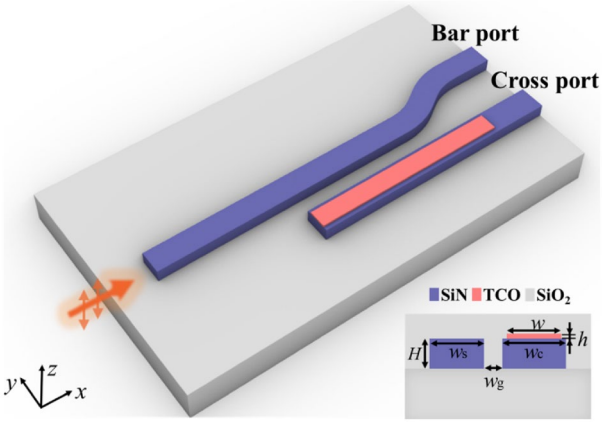

Figure 1. Perspective and cross-sectional view of the designed all-optical switch system. The proposed design includes an input waveguide and an ENZ TCO-loaded waveguide. The bar port and the cross port are outputs of the input waveguide and the TCO-loaded waveguide, respectively.

dedicatedly designed all-optical device based on the silicon nitride waveguide platform yields performance of low insertion loss (IL), low crosstalk (CT), broad bandwidth, as well as ultrafast optical response.

Results and discussions

Working principle of all-optical switching in epsilon-near-zero asymmetric directional coupler. Figure 1 shows the perspective view and cross-sectional view of the proposed switch based on ADC. The switch system consists of two adjacent, parallel silicon nitride (SiN) waveguides: an input waveguide and a TCO-loaded waveguide. Geometric parameters are marked in the cross-sectional view, in which H is the height of the two waveguides, h and w are the height and width of TCO layer, w_g is the distance between the two waveguides, w_s and w_c are the width of the input waveguide and the TCO-loaded waveguide, respectively. The ENZ TCO features large refractive index change, electric field enhancement, and ultrafast nonlinear response under excitation of pump light, such optical properties can be applied to the directional coupler by elaborate design. In the scheme of the proposed all-optical switch, an out-of-plane TM-polarized pump pulse is employed to induce a change of refractive index in TCO layer, resulting in coupled and uncoupled states in the two-waveguide optical system. Under the static state, the difference in the effective index between the input waveguide and the TCO-loaded waveguide causes a phase mismatch due to the low index of TCO layer. Therefore, the launched guided mode is confined and propagates in the input waveguide. While TCO is excited to a larger refractive index by pump fluence, the effective indices of the two waveguides are identical and satisfy the condition of phase match. The launched guided mode in the input waveguide tends to couple to the TCO-loaded waveguide according to coupled-mode theory. Therefore, the structural parameters of the ADC are optimally chosen to ensure phase match in the coupled state and phase mismatch in the uncoupled state.

Optical nonlinearity of ENZ layer. In the near-infrared region, degenerately doped semiconductors TCOs exhibit metal-like properties. In general, the following Drude model can quantify its permittivity dispersion profile[13]:

$$\varepsilon(\omega) = \varepsilon_\infty - \frac{\omega_p^2}{\omega^2 + i\gamma\omega}, \tag{1}$$

where ε_∞ is high-frequency permittivity, γ is the damping frequency, ω is the angular frequency of light and ω_p is plasma frequency. Here, we describe the static optical response of TCO with values from the references[23,25], where $\varepsilon_\infty = 5.5$, $\gamma = 3.35 \times 10^{13}$ rad s^{-1}, $\omega_p = 2.85 \times 10^{15}$ rad s^{-1}. The real part of the permittivity has a zero-crossing at the wavelength of 1.55 μm.

The nonlinearity of TCO can be ascribable to modification in the energy distribution in its non-parabolic conduction band induced by pump, which can be written as $(\hbar^2 k^2/2\ m) = E + CE^2$[26,27]. After considering the non-parabolicity of the conduction band, the relation between the plasma frequency ω_p and the hot-electron temperature T_e of TCO can be calculated by Eq. (2) (see "Methods": "Non-parabolic conduction of TCO" section for details). The calculated temperature-dependent plasma frequency is shown in Fig. 2a, and the plasma frequency ω_p decreases with the increment of the hot-electron temperature T_e.

As intensively studied in the past, ENZ materials possess a pronounced angular-dependent nonlinearity response, which is associated with field enhancement occurring within the near-zero permittivity region[28]. Here, we calculate the field enhancement factor ($EF = |E_{TCO}|^2/|E_0|^2$, where E_0 is the incident electric field in the air and E_{TCO} is the electric field inside the TCO ENZ layer) as a function of wavelength and incident angle[11]. The pronounced angular-dependent nonlinearity of TCO is observed in ENZ region. For a p-polarized incident light, the enhancement of the electric field within the TCO film enables larger nonlinearity[11,13,28,29]. This angular dependence can be calculated by considering the wavelength- and angle-dependent field enhancement factor EF[11,13,29].

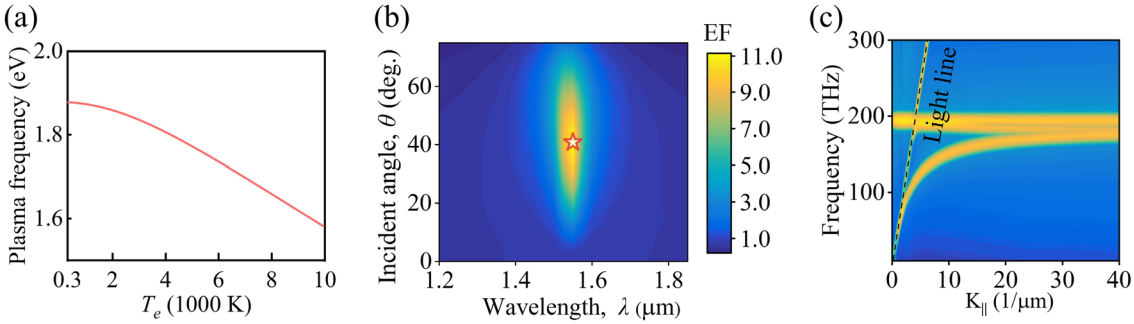

Figure 2. (**a**) Calculated plasma frequency ω_p as a function of hot-electron temperature T_e. (**b**) Simulated enhancement factor as a function of wavelength and incident angle. The red star symbol indicates a maximum value. (**c**) Dispersion relation of the TCO layer.

As shown in Fig. 2b, the field enhancement factor is up to 11.2-fold at an angle of 40° at ENZ wavelength, which is the largest nonlinearity that can be obtained in the ENZ TCO layer. Figure 2c further illustrates the dispersion relation of the TCO layer calculated by the finite-difference time-domain technique (Lumercial FDTD Solution). The calculation of bandstructure based on FDTD method is widely recognized and its accuracy has been verified[30–32]. In the FDTD bandstructure simulation of this work, a cloud of dipoles with different phases and orientations are placed inside the ENZ TCO film surrounded by a simulation region with Bloch boundary conditions. And the simulation time is set to be sufficiently long to ensure the appearance of modes that are supported by the ENZ TCO film. One can observe a nearly flat dispersion near 193.8 THz frequency, which is consistent with the maximum field EF at 1.55 μm (~ 193.4 THz). On the outside (right-hand side) of the light line cone, the thin ENZ film supports a long-range surface plasmon-polariton mode, which is known as ENZ mode for a thin ENZ film[30,33–36]. A leaky mode emerges on the inside (left-hand side) of the light line cone. The excitation of this leaky mode is related to the Berreman absorption for a thin film, thus it is known as the Berreman mode[33–35] or the Ferrell–Berreman mode[37]. The ENZ mode is a non-radiative mode which needs to be excited by coupling to localized plasmon resonances near the vertical component of electric field in ultrathin films of thickness $< \approx \lambda_{ENZ}/50$ with an additional coupling mechanism[34,36]. While the Ferrell–Berreman mode or Berreman mode is a radiative mode, it can be excited directly from the free space by a *p*-polarized light[34,36,38]. The large nonlinearity of ENZ media is associated with the enhancement of the electric filed[28]. While its enhancement mechanism originates from the continuity of the electric field, i.e., Maxwell's boundary conditions[11,28]. For the ENZ TCO film, a *p*-polarized light at oblique incidence from free space leads to the excitation of the Ferrell–Berreman mode at the ENZ wavelength of 1.55 μm, resulting in an electric field enhancement[13,33]. This eventually allows the existence of large nonlinearity of ENZ TCO under proper pump irradiation.

Furthermore, we utilize TTM (see "Methods" Two-temperature-model for details) to describe the temporal optical response of TCO. Based on TTM, change of dynamic hot-electron temperature T_e under pump fluence F can be derived, which can be later substituted into the non-parabolic conduction model to obtain the plasma frequency ω_p under different F. An increase in hot-electron temperature T_e will lead to a decreased ω_p and result in the modulation of permittivity of TCO. Consequently, refractive index n, absorption coefficient k, and their corresponding changes Δn, Δk can be obtained under different F based on the aforementioned results. Figure 3a,b show the refractive index n and absorption coefficient k of the ENZ TCO layer under various pump fluence F, while Fig. 3d,e further depict the changes of refractive index Δn and absorption coefficient Δk. One can observe both n and k have a larger modulation in the vicinity of ENZ spectral region. More specifically, the peak of Δn occurs at ~ 1.55 μm, manifesting the enhanced nonlinearity response induced by ENZ effect in the TCO layer. For the scheme of the all-optical ADC switch, the TCO layer exhibits a sufficient refractive index change Δn and a relatively low absorption coefficient k under $F = 0.0569$ mJ cm^{-2}, which allows coupling between the input waveguide and the TCO-loaded waveguide. Therefore, we opt for a pump fluence of 0.0569 mJ cm^{-2} in the following device design. The temporal response of refractive index n and absorption coefficient k at ENZ wavelength under $F = 0.0569$ mJ cm^{-2} shown in Fig. 3c reveals the ultrafast optical properties of the TCO layer. Figure 3f further illustrates the transient Δn response of the TCO layer. One can observe that the TCO layer has a rise time of ~ 109 fs and a recovery time of ~ 502 fs, corresponding to a high all-optical controlling speed of 1.35 THz in switching. To summarize, the ENZ TCO layer features a large refractive index change, low loss, and ultrafast transient response at ENZ wavelength.

Scheme design of the optical switch. Here, the two SiN waveguides are engineered to have identical height $H = 450$ nm, and w_c is set to 850 nm to ensure single-mode operation. The 60 nm-thick tunable TCO layer, which serves as a key component in the signal routing system is deposited on top of the waveguide. Considering the alignment precision of the electron-beam lithography, the width of TCO layer is chosen to be 100 nm narrower than the w_c[39,40]. The supportable guided modes in the TCO-loaded waveguide and the input waveguide can be calculated by mode solver based on the finite element method (Lumerical Mode Solution). The results indicate that the effective index of the TCO-loaded waveguide under the pump-off state $F = 0$ and the pump-on state $F = 0.0569$ mJ cm^{-2} are $1.498 + 0.012i$ and $1.575 + 0.003i$, respectively. The effective index of the input waveguide for various width w_s is shown in Fig. 4a. To ensure phase match between the TCO-loaded waveguide

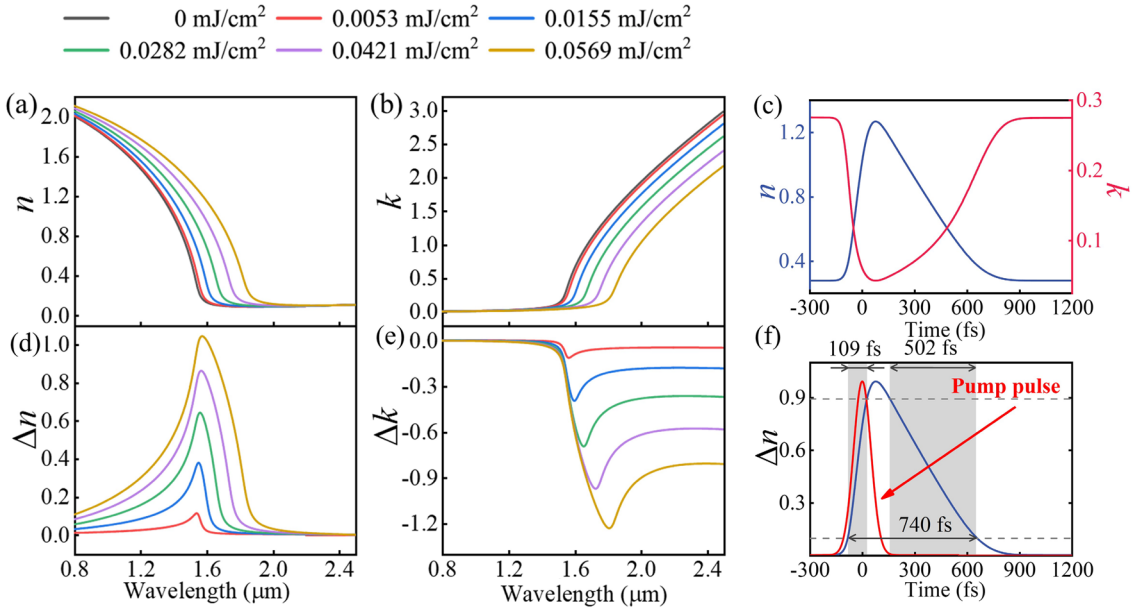

Figure 3. (**a**) Refractive index n, (**b**) absorption coefficient k, and (**c**) the transient response of n and k under $F = 0.0569$ mJ cm^{-2} at ENZ wavelength 1.55 μm. (**d**) The changes of refractive index Δn, (**e**) absorption coefficient Δk, and (**f**) the ultrafast change Δn in time domain at ENZ wavelength. The red curve denotes the pulse intensity profile (in arbitrary units).

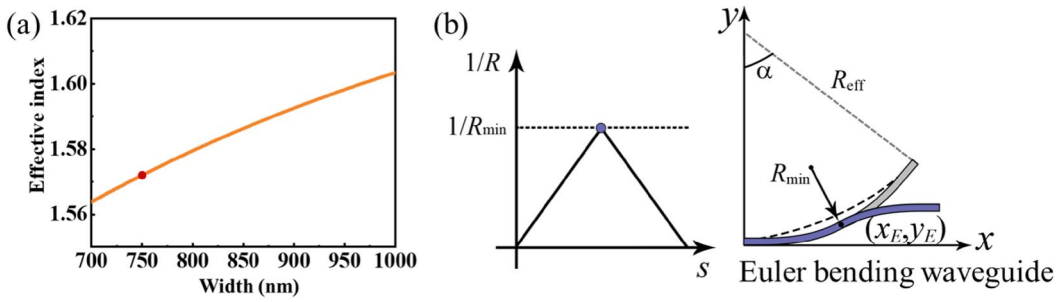

Figure 4. (**a**) Effective index of the TM mode as a function of width of the input waveguide w_s, the phase-match point marked with a red dot. (**b**) The basic concept of the Euler bending waveguide used in the configuration.

and the input waveguide under pump-on state, the input waveguide has to possess the same effective index as the TCO-loaded waveguide, thus w_s is set as 750 nm. At the end of the input waveguide, a designed Euler bending waveguide is utilized to make the two waveguides uncoupled. The Euler waveguide is a kind of bending waveguide designed on the basis of the mathematical Euler spiral, in which the curvature grows linearly with the curve length s, as shown in Fig. 4b. The curve length s is determined by $2R_{\min}\alpha$, where $R_{\min}$ denotes a given minimum curvature radius at the endpoint of (x_E, y_E) and α denotes a given angle. The whole Euler bending waveguide with length s consists of mirror-symmetric sections, each of them bends the light path by $\alpha/2$[41]. The use of the Euler curve contributes to the reduced bending loss and radiative loss when light is bent from straight to bending waveguide[42]. In our work, the designed bending part of the Euler curve waveguide is set as $R_{\min} = 20$ μm and $\alpha = 20°$.

Mode analysis. Figure 5a,b exhibit the modal intensity profile of quasi-transversal magnetic (TM) which can be supported by the single TCO-loaded waveguide in the pump-off state and pump-on state, respectively. Under the pump-off state, the TCO layer with a relatively low index forms a high-index-contrast structure with the SiN, leading to optical field confinement in the TCO layer. While for the pump-on state, the index of TCO is triggered to a relatively high value, allowing the optical field to be distributed mainly around the SiN waveguide. Supermode analyses are performed to give an illustration of the all-optical switching mechanism in the two-waveguide operation system. Figure 5c,d are the supermodes of the two-waveguide system in the pump-off state. Since the TCO layer operates under a low index, the effective index difference between the TCO-loaded waveguide and input waveguide results in phase mismatch, which isolates the two waveguides during light propagation. In contrast, the TCO layer is triggered to a relatively high index under pump excitation, making the

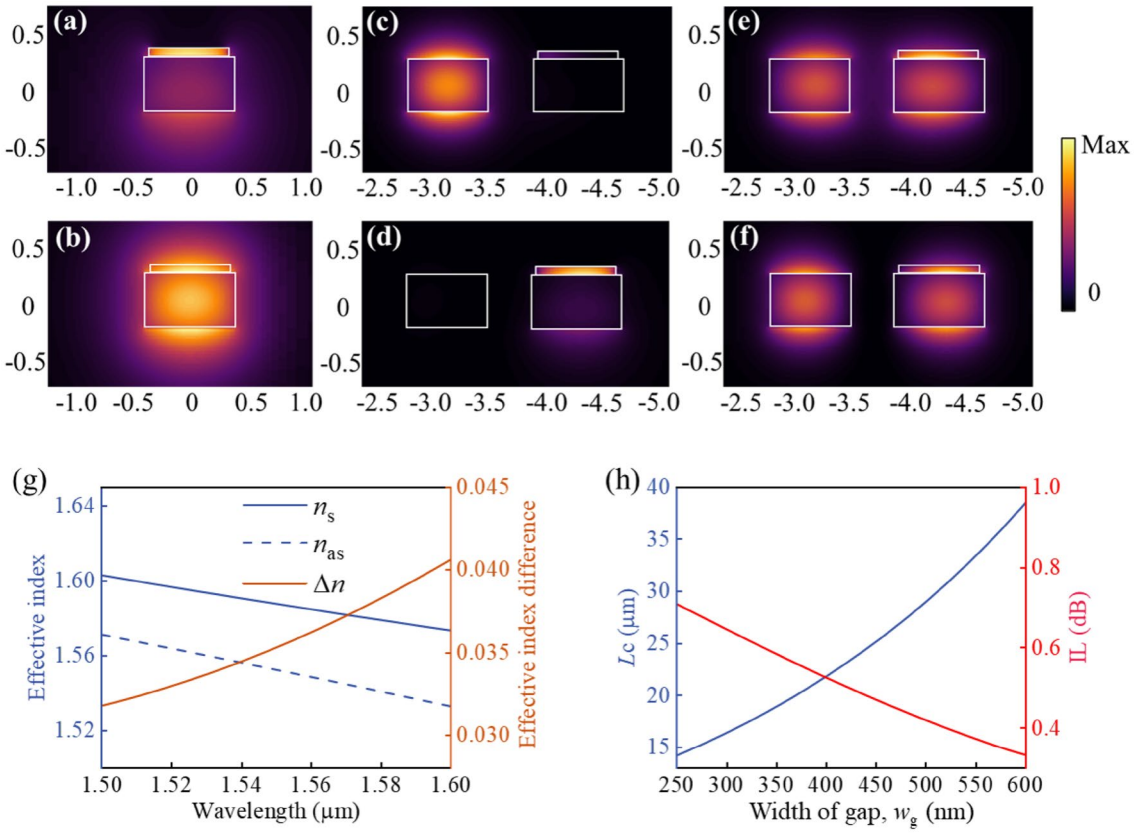

Figure 5. Mode field distribution of a SiN waveguide topped with the TCO layer in the (**a**) pump-off state and (**b**) pump-on state with pump fluence $F = 0.0569$ mJ cm^{-2}. The field intensity profile of a two-waveguide configuration with the TCO layer in the pump-off state (**c**,**d**), and in the pump-on state (**e**,**f**). (**g**) Effective index of the symmetric n_s and antisymmetric n_{as} supermodes as functions of wavelength in the pump-on state. (**h**) Coupling length L_c in the pump-on state and insertion loss IL in the pump-off state as a function of gap width w_g.

effective index of the two waveguides identical and satisfying phase match condition. The phase match therefore will induce strong coupling between the two waveguides with even and odd supermodes (Fig. 5e,f), also referred to as symmetric and antisymmetric modes. Note that the complex effective index of the even and odd supermodes are 1.592 + 0.0016i and 1.556 + 0.0018i, respectively. The simulated effective indices of symmetric mode n_s and antisymmetric mode n_{as} and the difference between (Δn) them as a function of wavelength are plotted in Fig. 5g. The coupling length L_c is determined by the relationship $L_c = \lambda/(2\Delta n)$, which means there is only one suitable coupling length for a given operation wavelength. Thus, the device designed for a specific wavelength cannot meet the coupling requirement perfectly at the other working wavelengths. For the working wavelength of 1.55 μm, the calculated coupling length of the proposed device $L_c = 21.5$ μm. Moreover, Fig. 5h indicates the increase of the width of the gap w_g leads to an increase of L_c in the pump-on state and a decrease of IL in the pump-off state. Considering the tradeoff between coupling length and IL, the gap width w_p is selected as 400 nm.

Transmission analysis. The light propagation property is analyzed based on finite-difference time-domain by Lumerical FDTD Solution. The field intensity distribution along the propagation direction of the proposed device in the pump-off state $F = 0$ is depicted in Fig. 6a. The TM-polarized light entirely remains in the input waveguide due to the phase mismatch between the two waveguides. Figure 6c shows the monitored transmission spectra of the Bar port and Cross port under $F = 0$. It is apparent that the optical switch achieves an IL = 1.02 dB and CT = − 18.93 dB at 1.55 μm. For the pump-on state $F = 0.0569$ mJ cm^{-2}, the phase match condition in the two-waveguide system is satisfied. As shown in Fig. 6b, it can be seen that the signal light initially propagates only in the input waveguide, and then is evanescently coupled and transferred to the TCO-loaded waveguide. Transmission spectra monitored at the output Cross port and Bar port show that the optical switch attains a low IL = 2.70 dB and a CT = − 19.54 dB at the communication wavelength of 1.55 μm, as shown in Fig. 6d.

Figure 7a shows the transmission spectrum of the proposed all-optical switch for various pump fluence F at 1.55 μm. One can observe that the increase in pump fluence F leads to a decrease in transmission at the Bar port while an increase in transmission at the Cross port. This results from the gradual increase of the TCO index with the increment of F, which allows more electrical field to be coupled into the TCO-loaded waveguide. Under pump fluence $F = 0.0569$ mJ cm^{-2}, the energy consumption of the switch for per bit is estimated as 14.6 pJ. In practical pump irritation, the illuminated spot will be larger than the designed layer, which leads to an increase in energy

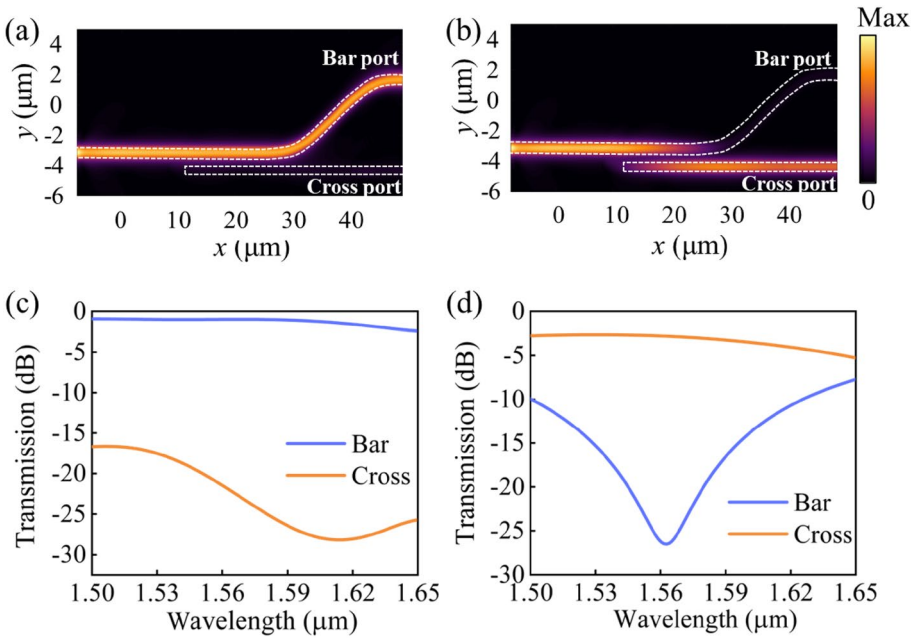

Figure 6. The normalized field intensity distribution along the propagation direction in the pump-off state (**a**) and pump-on state (**b**). Transmission spectra in the Cross port and Bar port in the pump-off state (**c**) and pump-on state (**d**).

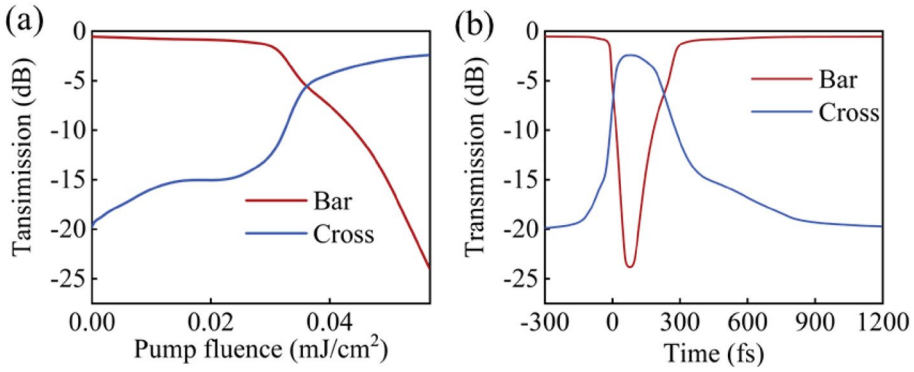

Figure 7. (**a**) Transmission versus pump fluence at the output Bar and Cross port. (**b**) Transient transmission at the output Bar and Cross port.

consumption per bit. The temporal response of the all-optical switch under $F = 0.0569$ mJ cm^{-2} is illustrated in Fig. 7b. Owing to the ultrafast transient response of the TCO layer, the device features a femtosecond magnitude of switching time. For the Cross port, a rising time of 121 fs and a falling time of 532 fs are obtained, while for the Bar port, a rising time of 163 fs and a falling time of 58 fs are attained. Here, the response time of this switch is strongly consistent with excitation and recovery of hot-electrons in the TCO layer. As extensively reported, ENZ effect utilized here is not limited to TCO layer and generally, it can be achieved by other approaches, for instance, plasmonic metamaterials which can effectively improve energy efficiency and make devices more compact. In summary, the modulation depth for the bar port is 18.93 dB, while that for the cross port is 19.54 dB. The all-optical switching system shows minimal 3-dB broadband over 1527–1594 nm, and features an ultrafast switching time of 221 fs for the bar port and 652 fs for the cross port. To better characterize the performance of the proposed device, we have summarized the recent works and compared the relevant work in recent years shown in Table 1. The proposed all-optical switch based on ADC exhibits the advantages of large modulation depth, wide bandwidth, and ultrafast switching speed. Noticeably, the interface between CdO and silicon nitride causes scattering across grain boundaries and increases the Drude-damping, which leads to an increase of the insertion loss of the proposed device[43,44]. On the other hand, the existence of the phononic interfacial thermal resistance causes the electron–phonon nonequilibrium near the interface between TCO and SiN. The undesired

Type	Structure	Modulation depth	Bandwidth	Speed	Energy consumption	References
Electro-absorption modulator	Slot waveguide (graphene)	1.6 dB μm^{-1}	≥6.8 GHz	N.A	418 fJ bit^{-1}	46, 47
Electro-optical switch	Hyperbolic metamaterial	26 dB	N.A	500 MHz	2.5 aJ bit^{-1}	48
All-optical modulator	Strip waveguide (hyperbolic metamaterial)	6.33 dB μm^{-1}	N.A	9.1 ps	3.7 pJ bit^{-1}	49
All-optical switch	Metal–insulator–metal nanocavity	120% reflectivity modulation	400 GHz	3 ps	5.2 mJ cm^{-2}	50
All-optical modulator	2D hybrid perovskites	2% reflectivity modulation	N.A	20 fs	20 pJ μm^{-2}	51
All-optical modulator	Microring resonator ($PtSe_2$)	~5 dB	2.4 kHz	284 us	210 mW	52
All-optical modulator	Strip waveguide (VO_2)	1.68 dB μm^{-1}	~12.5 THz	~ns	6.4 pJ bit^{-1}	10
All-optical switch	Au/CdO/HfO_2/Si capacitor	15.9 dB μm^{-1}	N.A	230 fs	13.5 fJ bit^{-1}	53
Optical switch	Directional coupler (GST)	22 dB (cGST) 10 dB (aGST) coupling length: ~30 μm	30 nm	N.A	2 nJ bit^{-1}	39
Optical switch	Directional coupler (GSST)	50 dB (crystalline state) 27 dB (amorphous state) coupling length: 40 μm	N.A	N.A	N.A	40
All-optical switch	Directional coupler (ENZ TCO)	18.93 dB (bar) 19.54 dB (cross) footp coupling length: 21.5 μm	8.25 THz	221 fs (bar) 653 fs (cross)	14.6 pJ bit^{-1}	This work

Table 1. Performance comparison with recent works.

effect reduces the hot electron cooling with a weaker electron–phonon coupling coefficient gep, which may lead to a longer nonlinear response time near the interface[45].

Conclusion

In conclusion, we have numerically demonstrated an all-optical switch based on ADC using ENZ effect on SiN platform. By calculation, in the ENZ region, this intensity-dependent refractive index and ultrafast transient response of the TCO layer under different pump fluence are assessed. The mode and 3D transmission analyses are used to investigated the performance of the device. The results show that, under an excitation pump fluence of 0.0569 mJ cm^{-2} at telecom wavelength, the switch features low insertion loss, low crosstalk, broadband, and ultrafast transition time both in the pump-off and pump-on state near ENZ region. The results of this work demonstrate for the first time the application of the ENZ effect in integrated waveguide switch, offering a possibility for the design of switching components in high-speed all-optical signal processing chips.

Methods

Non-parabolic conduction of TCO. The plasma frequency ω_p can be written as[27]:

$$\omega_p(T_e)^2 = \frac{e^2}{3m\pi^2}\int_0^\infty dE\left(\frac{2m}{\hbar^2}(E+CE^2)\right)^{\frac{3}{2}}(1+2CE)^{-1}\left(-\frac{\partial f_0(E,T_e)}{\partial E}\right), \tag{2}$$

where $m = 0.12\ m_0$ (m_0 the free electron mass), $\hbar$ is the reduced Plank's constant, $C = 0.34\ eV^{-1}$[19] determines the structure of non-parabolic conduction, and the function $f_0(E, T_e)$ is the Fermi–Dirac distribution function determined by electron temperature T_e and the electron energy E. Here, electron-temperature-dependence of f_0 is mainly due to the fact that T_e can produce a change in electro-chemical potential and thereby modifying Fermi–Dirac function. Note that, the modification of the Fermi–Dirac distribution induced by T_e is more markable in degenerately doped semiconductors than in noble metals. The reasons originate from the lower heat capacity of electrons in CdO as well as its non-parabolic conduction structure. Therefore, the phenomenon gives rise to an electron-temperature-dependent plasma frequency $\omega_p(T_e)$.

Two-temperature-model. To calculate the transient response of the TCO layer, the following two-temperature model is used[11,27]:

$$\begin{aligned} C_e(T_e)\frac{\partial T_e(t)}{\partial t} &= -g_{ep}(T_e(t)-T_l(t)) + \frac{N(t)}{\tau_{ee}(t)},\\ C_l\frac{\partial T_l(t)}{\partial t} &= g_{ep}(T_e(t)-T_l(t)) + \frac{N(t)}{\tau_{ep}(t)},\\ \frac{\partial N(t)}{\partial t} &= -\frac{N(t)}{\tau_{ee}(t)} - \frac{N(t)}{\tau_{ep}(t)} + P(t), \end{aligned} \tag{3}$$

where T_l is the lattice temperature, τ_{ee} (τ_{ep}) is the electron–electron (electron–phonon) relaxation time, and C_e (C_l) is the heat capacity of free electron (lattice). N is the non-thermal energy density stored in the excited electrons, and g_{ep} denotes the electron–phonon coupling coefficient. Here, P is time-dependent absorbed energy in the material, and C_e, g_{ep}, P can be expressed as follow respectively[11]:

$$C_e = \frac{3\pi^2 n_e k_B T_e}{\sqrt{36T_F^2 + 4\pi^4 T_e^2}}, \tag{4}$$

$$g_{ep}=0.562 n_e \frac{k_B^2 \Theta_D^2 \nu_F}{L_f T_l E_F}, \tag{5}$$

$$P(t) = \frac{F}{\tau_p}\alpha e^{-2\left(\frac{t}{\tau_p}\right)^2}. \tag{6}$$

In Eq. (4), k_B is the Boltzmann constant; $n_e = 6.1 \times 10^{20}$ cm^{-3} is the total number electrons in the conduction band and maintained as a constant under a proper thermal excitation; and T_F is the Fermi temperature obtained from Ref.[27]. In Eq. (5), Θ_D is the Debye temperature[54], ν_F is the Fermi velocity[55], E_F is the Fermi level and L_f is the electron mean free path[56]. In Eq. (6), F is the pump fluence, τ_p is the pump pulse duration set as 100 fs and α is the attenuation coefficient of CdO estimated from Ref.[57]. In the calculation of TTM, consider that the lattice has a much higher heat capacity C_l of than the heat capacity of electron C_e, we can take it as a constant with $C_l = 2.9 \times 10^6$ J·m^{-3} K^{-1}[58].

Data availability

The data that support the findings of this study are available from the corresponding author upon resonable request.

Received: 31 May 2022; Accepted: 17 October 2022
Published online: 26 October 2022

References

1. Feldmann, J. *et al.* Calculating with light using a chip-scale all-optical abacus. *Nat. Commun.* **8**, 1256. https://doi.org/10.1038/s41467-017-01506-3 (2017).
2. Feldmann, J., Youngblood, N., Wright, C. D., Bhaskaran, H. & Pernice, W. H. P. All-optical spiking neurosynaptic networks with self-learning capabilities. *Nature* **569**, 208–214. https://doi.org/10.1038/s41586-019-1157-8 (2019).
3. Tsang, H. K. *et al.* Optical dispersion, two-photon absorption and self-phase modulation in silicon waveguides at 1.5μm wavelength. *Appl. Phys. Lett.* **80**, 416–418. https://doi.org/10.1063/1.1435801 (2002).
4. Almeida, V. R., Barrios, C. A., Panepucci, R. R. & Lipson, M. All-optical control of light on a silicon chip. *Nature* **431**, 1081–1084. https://doi.org/10.1038/nature02921 (2004).
5. Nozaki, K. *et al.* Sub-femtojoule all-optical switching using a photonic-crystal nanocavity. *Nat. Photon.* **4**, 477–483. https://doi.org/10.1038/nphoton.2010.89 (2010).
6. Ooi, K. J. A., Leong, P. C., Ang, L. K. & Tan, D. T. H. All-optical control on a graphene-on-silicon waveguide modulator. *Sci. Rep.* **7**, 12748. https://doi.org/10.1038/s41598-017-13213-6 (2017).
7. Wang, Y. *et al.* All-optical phosphorene phase modulator with enhanced stability under ambient conditions. *Laser Photon. Rev.* **12**, 1–9. https://doi.org/10.1002/lpor.201800016 (2018).
8. Yang, S. *et al.* CMOS-compatible WS2-based all-optical modulator. *ACS Photon.* **5**, 342–346. https://doi.org/10.1021/acsphotonics.7b01206 (2018).
9. Stegmaier, M., Ríos, C., Bhaskaran, H., Wright, C. D. & Pernice, W. H. P. Nonvolatile all-optical 1 × 2 switch for chipscale photonic networks. *Adv. Opt. Mater.* **5**, 1600346. https://doi.org/10.1002/adom.201600346 (2017).
10. Wong, H. M. K. *et al.* Broadband, integrated, micron-scale, all-optical Si3N4/VO2 modulators with pj switching energy. *ACS Photon.* **6**, 2734–2740. https://doi.org/10.1021/acsphotonics.9b00708 (2019).
11. Alam, M. Z., De Leon, I. & Boyd, R. W. Large optical nonlinearity of indium tin oxide in its epsilon-near-zero region. *Science* **352**, 795–797. https://doi.org/10.1126/science.aae0330 (2016).
12. Caspani, L. *et al.* Enhanced nonlinear refractive index in ϵ-near-zero materials. *Phys. Rev. Lett.* **116**, 233901. https://doi.org/10.1103/PhysRevLett.116.233901 (2016).
13. Yang, Y. *et al.* Femtosecond optical polarization switching using a cadmium oxide-based perfect absorber. *Nat. Photon.* **11**, 390–395. https://doi.org/10.1038/nphoton.2017.64 (2017).
14. Wu, J., Xie, Z. T., Sha, Y., Fu, H. Y. & Li, Q. Epsilon-near-zero photonics: Infinite potentials. *Photon. Res.* **9**, 1616. https://doi.org/10.1364/PRJ.427246 (2021).
15. Baev, A., Prasad, P. N., Alam, M. Z. & Boyd, R. W. Dynamically controlling local field enhancement at an epsilon-near-zero/dielectric interface via nonlinearities of an epsilon-near-zero medium. *Nanophotonics* **9**, 4831–4837. https://doi.org/10.1515/nanoph-2020-0490 (2020).
16. Wu, J., Xie, Z. T., Sha, Y., Fu, H. Y. & Li, Q. Comparative study on epsilon-near-zero transparent conducting oxides: High-order chromatic dispersions and modeling of ultrashort pulse interactions. *Phys. Rev. A* **102**, 1–7. https://doi.org/10.1103/PhysRevA.102.053503 (2020).
17. Sha, Y., Wu, J., Xie, Z. T., Fu, H. Y. & Li, Q. Comparison study of multi-slot designs in epsilon-near-zero waveguide-based electro-optical modulators. *IEEE Photon. J.* **13**, 1–12. https://doi.org/10.1109/JPHOT.2021.3084943 (2021).
18. Huang, Y. *et al.* High-bandwidth Si/In 2 O 3 hybrid plasmonic waveguide modulator. *APL Photon.* **7**, 051301. https://doi.org/10.1063/5.0087540 (2022).
19. Hu, F., Jia, W., Meng, Y., Gong, M. & Yang, Y. High-contrast optical switching using an epsilon-near-zero material coupled to a Bragg microcavity. *Opt. Express* **27**, 26405. https://doi.org/10.1364/oe.27.026405 (2019).
20. Guo, P. *et al.* Large optical nonlinearity of ITO nanorods for sub-picosecond all-optical modulation of the full-visible spectrum. *Nat. Commun.* **7**, 12892. https://doi.org/10.1038/ncomms12892 (2016).
21. Xie, Z. T., Wu, J., Fu, H. Y. & Li, Q. Tunable electro-and all-optical switch based on epsilon-near-zero metasurface. *IEEE Photon. J.* **12**, 4501510. https://doi.org/10.1109/JPHOT.2020.3010284 (2020).
22. Bohn, J. *et al.* All-optical switching of an epsilon-near-zero plasmon resonance in indium tin oxide. *Nat. Commun.* **20**, 1–6 (2021).
23. Navarro-Arenas, J., Parra, J. & Sanchis, P. Ultrafast all-optical phase switching enabled by epsilon-near-zero materials in silicon. *Opt. Express* **30**, 14518. https://doi.org/10.1364/OE.454181 (2022).

24. Parra, J., Pernice, W. H. P. & Sanchis, P. All-optical phase control in nanophotonic silicon waveguides with epsilon-near-zero nanoheaters. *Sci. Rep.* **11**, 1–9. https://doi.org/10.1038/s41598-021-88865-6 (2021).
25. Reines, I. C., Wood, M. G., Luk, T. S., Serkland, D. K. & Campione, S. Compact epsilon-near-zero silicon photonic phase modulators. *Opt. Express* **26**, 21594. https://doi.org/10.1364/oe.26.021594 (2018).
26. Alam, M. Z., Schulz, S. A., Upham, J., De Leon, I. & Boyd, R. W. Large optical nonlinearity of nanoantennas coupled to an epsilon-near-zero material /639/624/399/1015 /639/624/400/385 letter. *Nat. Photon.* **12**, 79–83. https://doi.org/10.1038/s41566-017-0089-9 (2018).
27. Guo, P., Schaller, R. D., Ketterson, J. B. & Chang, R. P. H. Ultrafast switching of tunable infrared plasmons in indium tin oxide nanorod arrays with large absolute amplitude. *Nat. Photon.* **10**, 267–273. https://doi.org/10.1038/nphoton.2016.14 (2016).
28. Reshef, O., De Leon, I., Alam, M. Z. & Boyd, R. W. Nonlinear optical effects in epsilon-near-zero media. *Nat. Rev. Mater.* **4**, 535–551. https://doi.org/10.1038/s41578-019-0120-5 (2019).
29. Yang, Y. *et al.* High-harmonic generation from an epsilon-near-zero material. *Nat. Phys.* **15**, 1022–1026. https://doi.org/10.1038/s41567-019-0584-7 (2019).
30. Manukyan, K. *et al.* Dependence of the coupling properties between a plasmonic antenna array and a sub-wavelength epsilon-near-zero film on structural and material parameters. *Appl. Phys. Lett.* **118**, 241102. https://doi.org/10.1063/5.0042599 (2021).
31. Ghindani, D., Rashed, A. R., Habib, M. & Caglayan, H. Gate tunable coupling of epsilon-near-zero and plasmonic modes. *Adv. Opt. Mater.* **9**, 2100800. https://doi.org/10.1002/adom.202100800 (2021).
32. Galfsky, T., Gu, J., Narimanov, E. E. & Menon, V. M. Photonic hypercrystals for control of light-matter interactions. *Proc. Natl. Acad. Sci. USA* **114**, 5125–5139. https://doi.org/10.1073/pnas.1702683114 (2017).
33. Passler, N. C. *et al.* Second harmonic generation from phononic epsilon-near-zero Berreman modes in ultrathin polar crystal films. *ACS Photon.* **6**, 1365–1371. https://doi.org/10.1021/acsphotonics.9b00290 (2019).
34. Vassant, S., Hugonin, J.-P., Marquier, F. & Greffet, J.-J. Berreman mode and epsilon near zero mode. *Opt. Express* **20**, 23971. https://doi.org/10.1364/oe.20.023971 (2012).
35. Liu, C. *et al.* Photon acceleration using a time-varying epsilon-near-zero metasurface. *ACS Photon.* **8**, 716–720. https://doi.org/10.1021/acsphotonics.0c01929 (2021).
36. Campione, S., Brener, I. & Marquier, F. Theory of epsilon-near-zero modes in ultrathin films. *Phys. Rev. B* **91**, 121408. https://doi.org/10.1103/PhysRevB.91.121408 (2015).
37. Newman, W. D. *et al.* Ferrell–Berreman modes in plasmonic epsilon-near-zero media. *ACS Photon.* **2**, 2–7. https://doi.org/10.1021/ph5003297 (2015).
38. Almossalami, H. A. *et al.* Sub-bandgap light absorption enhancement in germanium films through Berreman mode weak coupling to a microcavity mode. *Opt. Express* **29**, 44189. https://doi.org/10.1364/oe.445626 (2021).
39. Xu, P., Zheng, J., Doylend, J. K. & Majumdar, A. Low-loss and broadband nonvolatile phase-change directional coupler switches. *ACS Photon.* **6**, 553–557. https://doi.org/10.1021/acsphotonics.8b01628 (2019).
40. Zhang, Q. *et al.* Broadband nonvolatile photonic switching based on optical phase change materials: Beyond the classical figure-of-merit. *Opt. Lett.* **43**, 94. https://doi.org/10.1364/ol.43.000094 (2018).
41. Cherchi, M. *et al.* The Euler bend: Paving the way for high-density integration on micron-scale semiconductor platforms. In *Proceedings of SPIE* 899004. (2014).
42. Vogelbacher, F. *et al.* Analysis of silicon nitride partial Euler waveguide bends. *Opt. Express* **27**, 31394. https://doi.org/10.1364/oe.27.031394 (2019).
43. Sachet, E. *et al.* Dysprosium-doped cadmium oxide as a gateway material for mid-infrared plasmonics. *Nat. Mater.* **14**, 414–420. https://doi.org/10.1038/nmat4203 (2015).
44. Saha, S. *et al.* Broadband, high-speed, and large-amplitude dynamic optical switching with yttrium-doped cadmium oxide. *Adv. Funct. Mater.* **30**, 1–7. https://doi.org/10.1002/adfm.201908377 (2020).
45. Wang, Y. *et al.* Effect of interlayer on interfacial thermal transport and hot electron cooling in metal-dielectric systems: An electron-phonon coupling perspective. *J. Appl. Phys.* https://doi.org/10.1063/1.4941347 (2016).
46. Wu, Z. & Xu, Y. Design of a graphene-based dual-slot hybrid plasmonic electro-absorption modulator with high-modulation efficiency and broad optical bandwidth for on-chip communication. *Appl. Opt.* **57**, 3260–3267. https://doi.org/10.1364/ao.57.003260 (2018).
47. Liu, S., Xu, K., Song, Q., Cheng, Z. & Tsang, H. K. Design of mid-infrared electro-optic modulators based on aluminum nitride waveguides. *Opt. Lett.* **41**, 2501–2504. https://doi.org/10.1109/JLT.2016.2587319 (2016).
48. Caligiuri, V. *et al.* Near- and mid-infrared graphene-based photonic architectures for ultrafast and low-power electro-optical switching and ultra-high resolution imaging. *ACS Appl. Nano Mater.* **3**, 12218–12230. https://doi.org/10.1021/acsanm.0c02690 (2020).
49. Neira, A. D., Wurtz, G. A., Ginzburg, P. & Zayats, A. V. Ultrafast all-optical modulation with hyperbolic metamaterial integrated in Si photonic circuitry. *Opt. Express* **22**, 10987. https://doi.org/10.1364/oe.22.010987 (2014).
50. Kuttruff, J. *et al.* Ultrafast all-optical switching enabled by epsilon-near-zero-tailored absorption in metal-insulator nanocavities. *Commun. Phys.* **3**, 114. https://doi.org/10.1038/s42005-020-0379-2 (2020).
51. Grinblat, G. *et al.* Ultrafast all-optical modulation in 2D hybrid perovskites. *ACS Nano* **13**, 9504–9510. https://doi.org/10.1021/acsnano.9b04483 (2019).
52. Wei, K. *et al.* All-optical PtSe 2 silicon photonic modulator with ultra-high stability. *Photon. Res.* **8**, 1189. https://doi.org/10.1364/prj.392512 (2020).
53. Li, E. & Wang, A. X. Femto-Joule all-optical switching using epsilon-near-zero high-mobility conductive oxide. *IEEE J. Sel. Top. Quantum Electron.* **27**, 1–9. https://doi.org/10.1109/JSTQE.2020.3018104 (2021).
54. Munawar, T. *et al.* Synthesis of novel heterostructured ZnO-CdO-CuO nanocomposite: Characterization and enhanced sunlight driven photocatalytic activity. *Mater. Chem. Phys.* **249**, 122983. https://doi.org/10.1016/j.matchemphys.2020.122983 (2020).
55. de Ceglia, D. *et al.* Viscoelastic optical nonlocality of low-loss epsilon-near-zero nanofilms. *Sci. Rep.* **8**, 9335. https://doi.org/10.1038/s41598-018-27655-z (2018).
56. Vasheghani Farahani, S. K. *et al.* Electron mobility in CdO films. *J. Appl. Phys.* **109**, 25. https://doi.org/10.1063/1.3562141 (2011).
57. Gupta, R. K., Ghosh, K., Patel, R. & Kahol, P. K. Bandgap engineering of rare earth element doped nanostructured cadmium oxide thin films. *Phys. E Low-Dimensional Syst. Nanostruct.* **44**, 163–167. https://doi.org/10.1016/j.physe.2011.08.009 (2011).
58. Bardadym, Y. & Sporyagin, E. The influence of the constant physical fields on structure of polymer composites with cadmium oxide and polyaniline. In *Proceedings of 2017 IEEE 7th International Conference on Nanomaterials: Properties and Their Applications 2017* **2017-Janua**, 3–7. https://doi.org/10.1109/NAP.2017.8190261 (2017).

Acknowledgements

This work is supported by Basic and Applied Basic Research Foundation of Guangdong Province (2021A1515012176); Shenzhen Fundamental Research Program (GXWD20201231165807007-20200827130534001); Youth Science and Technology Innovation Talent of Guangdong Province (2019TQ05X227).

Author contributions

Y.S., Z.T.X., J.W., and Q.L. conceived the idea. Y.S., Z.T.X., and J.W. performed device simulation, and H.Y.F. provided simulation resources. All authors discussed the data. Y.S. and Q.L. wrote the manuscript with input from others. Q.L. supervised the project. All authors reviewed the manuscript.

Competing interests

The authors declare no competing interests.

Additional information

Correspondence and requests for materials should be addressed to Q.L.

Reprints and permissions information is available at www.nature.com/reprints.

Publisher's note Springer Nature remains neutral with regard to jurisdictional claims in published maps and institutional affiliations.